On the Electronic Structure of *mer,trans*-[RuCl$_3$(1*H*-indazole)$_2$(NO)], a Hypothetical Metabolite of the Antitumor Drug Candidate KP1019: An Experimental and DFT Study

**Lukas Bučinský,*[a] Gabriel E. Büchel,[b] Robert Ponec,[c]
Peter Rapta,[a] Martin Breza,[a] Jozef Kožíšek,[a] Marian Gall,[d]
Stanislav Biskupič,[a] Marek Fronc,[a] Katharina Schiessl,[b]
Olesea Cuzan,[e] Denis Prodius,[e] Constantin Turta,[e]
Sergiu Shova,[e,f] Dariusz A. Zając,[g,h] and Vladimir B. Arion*[b]**

The study reported herein focused on the electronic structure of the {Ru(NO)}^{6} fragment and characterization of the oxidation state of ruthenium in *mer,trans*-[RuCl$_3$(Hind)$_2$(NO)] (**1**; Hind = 1*H*-indazole) resulting from the reaction of *mer,trans*-[RuCl$_3$(H$_2$O)(Hind)$_2$] (**2**) with NO in acetone or solid-state Anderson rearrangement of (H$_2$ind)$_2$[RuCl$_5$(NO)] at 180 °C. The results of X-ray diffraction, ^{1}H, ^{13}C, and ^{15}N NMR, EPR, IR, and UV/Vis spectroscopy, cyclic voltammetry, magnetic susceptibility, and XANES/EXAFS as well as theoretical data have been critically analyzed. The localized orbitals, domain-averaged Fermi holes, frontier orbitals, Mulliken population, and quantum theory of atoms-in-molecules (QTAIM) analyses are presented. In addition, *mer,trans*-[Ru^{III}Cl$_3$(H$_2$O)(Hind)$_2$] (**2**) and *trans*-[Ru^{II}Cl$_2$(Hind)$_4$] (**3**) were experimentally and theoretically investigated as reference compounds. A complete active space SCF calculation was performed to estimate the extent of antiferromagnetic spin–spin coupling in **1**. We found that the closed-shell structure {Ru^{III}(NO)^0}^{6} fits better to the physical/spectroscopic properties of **1**, although {Ru^{II}(NO)$^+$}^{6} is formally still suitable for describing the oxidation state of Ru in this entity.

[a] Slovak University of Technology, Institute of Physical Chemistry and Chemical Physics,
Radlinského 9, 81237 Bratislava, Slovakia
E-mail: lukas.bucinsky@stuba.sk
Homepage: http://www.fchpt.stuba.sk/english/institutes-and-departments/institute-of-physical-chemistry-and-chemical-physics/department-of-chemical-physics.Ahtml?page_id=2211
[b] University of Vienna, Institute of Inorganic Chemistry,
Währinger Str. 42, 1090 Vienna, Austria
E-mail: vladimir.arion@univie.ac.at
Homepage: http://anorg-chemie.univie.ac.at/magnoliaPublic/Research/Bioinorganic-chemistry/Researchers/Arion.html
[c] Institute of Chemical Process Fundamentals, Academy of Sciences of the Czech Republic v.v.i.,
Suchdol 2, 16502 Prague 6, Czech Republic
[d] Slovak University of Technology, Institute of Information Engineering, Automation and Mathematics,
Radlinského 9, 81237 Bratislava, Slovakia
[e] Institute of Chemistry of the Academy of Sciences of Moldova,
Academiei str. 3, 2028 Chishinau, Moldova
[f] Moldova State University,
Mateevici str. 60, 2009 Chishinau, Moldova
[g] Helmholtz-Zentrum Berlin für Materialien und Energie GmbH, Institute of Solar Fuels,
Hahn-Meitner-Platz 1, 14109 Berlin, Germany
[h] HASYLAB at Deutsches Elektronen-Synchrotron, Research Centre of the Helmholtz Association,
Notkestr. 85, 22607 Hamburg, Germany

Introduction

Ruthenium(II) and ruthenium(III) classical coordination compounds as well as organoruthenium(II) complexes are promising anticancer drug candidates.[1] The two most prominent investigational drugs, namely (H$_2$ind)[Ru^{III}Cl$_4$(Hind)$_2$] (Hind = 1*H*-indazole, KP1019)[2] and (H$_2$im)[Ru^{III}Cl$_4$(dmso)(Him)] (Him = 1*H*-imidazole, NAMI-A),[3] are currently in phase I–II clinical trials. The prodrug *trans*-[Ru^{III}Cl$_4$(Hind)$_2$]$^-$ is active as an anticancer agent against primary tumors and metastases and, in particular, colon carcinomas.[4] Although its antitumor activity was reported about 30 years ago, the mechanism of action remains obscure, at least at the molecular level, and identification of its active species is of major interest. Aquation of the prodrug results in the formation of the reactive species *mer,trans*-[Ru^{III}Cl$_3$(H$_2$O)(Hind)$_2$] with a labile Ru–OH$_2$ bond. This compound was found to undergo dimerization in poorly coordinating solvents such as acetone or thf with the formation of [Ru^{III}Cl$_2$(μ-Cl)(Hind)$_2$]$_2$.[5] Both species have been characterized by spectroscopic methods and X-ray crystallography.

The anti-angiogenic and anti-invasive properties of NAMI-A have been attributed to the NO-capturing mechanism responsible for metastasis control of this investigational drug.[6] The high affinity of ruthenium for NO is well

documented in the literature.[7] The pronounced effect of NAMI-A on angiogenesis was confirmed in the chick allantoic membrane and in the rabbit eye cornea model.[8,9] It should be also noted that NO, which is produced by a number of nitric oxide synthase (NOS) enzymes from L-arginine in the body,[10] plays a major role as a signaling molecule in biological signal transducing systems, for example, in blood pressure regulation,[11,12] neurotransmission,[13,14] inflammatory response,[15,16] as well as necrosis[17] and apoptosis.[18,19] Nitric oxide is therefore essential in biological systems, but both its excess as well as deficiency leads to pathologies.

Furthermore, NO acts as a non-innocent ligand in coordination chemistry,[20,21] which renders the description of the exact electronic structure of the metal–NO entity difficult. Almost four decades ago, Enemark and Feltham[22] offered a useful approach for describing the electronic structure of metal–nitrosyl species as $\{M(NO)\}^n$ [n being the total number of electrons in the d (metal) and π^* (NO) orbitals]. However, this notation leaves the actual physical and formal oxidation state[23] of the metal center and nitrosyl ligand unclear, and therefore it remains a subject of notable interest.[24–37] This study is an attempt to describe such a $\{Ru(NO)\}^6$-containing system in more detail.

Herein we report on the synthesis, spectroscopic, magnetic, and cyclic voltammetry studies of *mer,trans*-$[RuCl_3(Hind)_2(NO)]$ (**1**) along with the electronic structure of **1** and two other related compounds, *mer,trans*-$[Ru^{III}Cl_3(H_2O)(Hind)_2]$ (**2**)[5] and *trans*-$[Ru^{II}Cl_2(Hind)_4]$ (**3**),[38] reported previously and now investigated by DFT methods. The physical and formal oxidation states of ruthenium in **1** are compared with those of **2** (Ru^{III}) and **3** (Ru^{II}). XANES and EXAFS experiments were performed to elucidate the physical oxidation state of the central metal in **1**. The localized orbitals (**1–3**) and DAFH analysis[39–41] (**1**) were used to further elucidate the electron structure of the $\{Ru(NO)\}^6$ fragment in **1**. QTAIM[42,43] and Mulliken population analyses (MPA) were performed to gain insight into the nature of the coordination bonds. The redox behavior of the studied species has been qualitatively considered by comparison of the HOMO–LUMO orbitals of the studied compounds. In addition, the possible antiferromagnetic interaction in the $\{Ru(NO)\}^6$ unit in **1** is briefly considered by means of a small complete active space SCF (CASSCF) calculation.

Results and Discussion

$[RuCl_3(Hind)_2(NO)]$ was readily synthesized in two ways: 1) By reaction with $[RuCl_3(H_2O)(Hind)_2]$ with gaseous NO in acetone and 2) by the solid-state Anderson rearrangement of $(H_2ind)[RuCl_5(NO)]$ at 180 °C. The indazolium salt was prepared by a metathesis reaction starting from $Na_2[RuCl_5(NO)]\cdot6H_2O$, which in turn was obtained by the reaction of $RuCl_3\cdot3H_2O$ with $NaNO_2$ in the presence of 1 M hydrochloric acid.

The IR spectrum of **1** shows a very strong absorption with a maximum at 1870 cm^{-1} (1832 cm^{-1} for the ^{15}NO-enriched sample) attributed to the NO stretching vibration. This value is comparable to a maximum at 1894 cm^{-1} for $Na_2[RuCl_5(NO)]\cdot6H_2O$ and implies that the NO ligand has nitrosonium or nitrosyl character.[44] Note that the v_{NO} value for free NO$^+$ is 2377 cm^{-1}, whereas that for NO is 1875 cm^{-1}.[45] The Ru–NO stretching vibration in **1** is at 587 cm^{-1} (586 cm^{-1} in the sodium salt), in agreement with those of a number of other ruthenium–nitrosyl compounds.[77] Stretching vibrations for $[Ru^{II}(hedeta)(Y)]^{n-}$ complexes [hedeta = N-(hydroxyethyl)ethylenediaminetriacetate] are reported at 1846, 1827, 1858, 1842, 1383, and 1370 cm^{-1} for Y = ^{14}NO$^+$, ^{15}NO$^+$, ^{14}NO, ^{15}NO, ^{14}NO$^-$, and ^{15}NO$^-$, respectively, and are in agreement with the linear coordination of NO$^+$ to Ru^{II} or NO^0 to Ru^{III} in **1**.[46]

The diamagnetic behavior of a polycrystalline sample of **1** and $Na_2[RuCl_5(NO)]\cdot6H_2O$ in the temperature range of 2–300 K in a magnetic field of 1 T provides further evidence for the formulation $\{Ru(NO)\}^6$ containing Ru^{II} ($S = 0$) bonded to NO$^+$ ($S = 0$) or NO^0 ($S = \frac{1}{2}$) coupled antiferromagnetically or through a closed-shell interaction to Ru^{III} ($S = \frac{1}{2}$).

The ^{1}H, ^{13}C, and ^{15}N NMR spectra of **1** show signals for indazole and the ^{15}N-labeled nitrosyl ligand (see Figures S1–S5 in the Supporting Information). The ^{1}H NMR spectrum is well resolved and displays identical signal sets for both coordinated indazoles (molecular symmetry C_2) with the same multiplicity as for the metal-free indazole, in line with the diamagnetism of **1** (see Figure S1). The H1 resonance in the ^{15}N,^{1}H HSQC plot is seen at $\delta = 13.77$ ppm (see Figure S4; for atomic labeling, see part a of Figure 1). Another singlet, attributed to H3, is observed at $\delta = 8.80$ ppm. The ^{1}H,^{13}C HMBC plot shows a cross-peak of C3 with H4. The cross-peaks in the ^{1}H,^{1}H COSY plot indicate H4–H5 and H6–H7 couplings (see Figure S5). Therefore two doublets are due to H7 ($\delta = 7.80$ ppm) and H4 ($\delta = 7.99$ ppm) protons, and two triplets have been assigned to H6 ($\delta = 7.58$ ppm) and H5 ($\delta = 7.31$ ppm). In the ^{13}C$\{^1$H$\}$ NMR spectrum (see Figure S2), four CH signals arising from C7, C4, C5, and C6 are seen at 111.58, 121.76, 122.80, and 129.77 ppm, respectively, and two carbon signals originate from the quaternary carbons C8 and C9. In the CH HMBC plot (see Figure S6), the CH at $\delta = 122.01$ ppm shows cross-peaks with H1, H3, H4, and H5, whereas the CH at $\delta = 141.51$ ppm reveals cross-peaks with H1, H3, H4, and H6. Taking into account the fact that the couplings through four bonds, such as C8–H5 and C9–H6, are most likely undetectable, we suppose that C8 displays a signal at $\delta = 141.51$ ppm and C9 at $\delta = 122.01$ ppm.

A ^{15}N resonance arising from the ^{15}NO-enriched sample of **1** appears at $\delta = 316$ ppm (see Figure S3 in the Supporting Information), which compares well with those measured for $Na_2[RuCl_5(^{15}NO)]\cdot6H_2O$ at $\delta = 313$ ppm and $[Ru(NO)(NH_3)_5]Cl_3$ at $\delta = 312$ ppm, determined relative to ^{15}NH$_4$Cl,[47] and suggests a linear coordination of NO$^+$ to ruthenium(II) or NO^0 to ruthenium(III). The nitrogen chemical shifts due to the bent coordination of NO$^-$ to ruthenium(II) documented in the literature are downshifted by several hundred ppm.[48] The linear coordination of NO$^+$
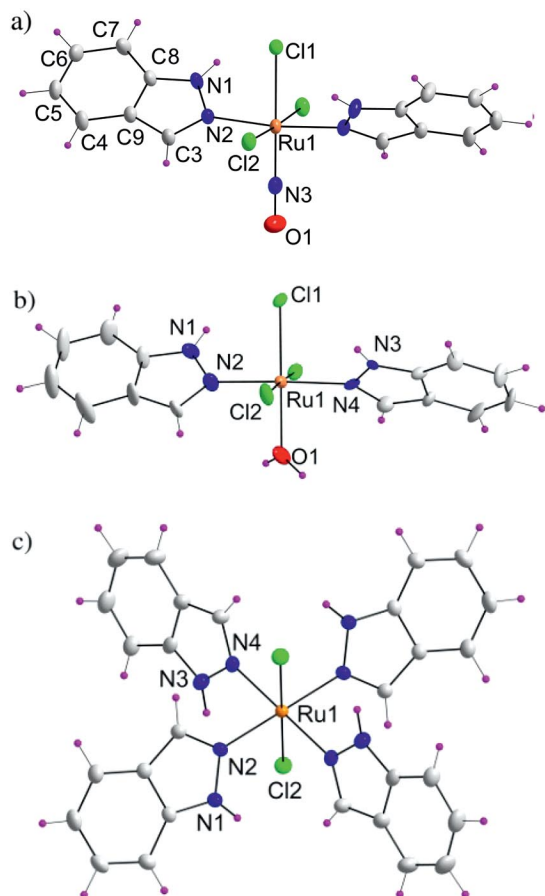
Figure 1. X-ray structures of the studied compounds with atom labeling schemes. a) [RuCl$_3$(Hind)$_2$(NO)] (**1**), b) [RuCl$_3$(H$_2$O)-(Hind)$_2$] (**2**), and c) [RuCl$_2$(Hind)$_4$] (**3**).

or NO^0 to ruthenium in **1** is further supported by the results of the X-ray diffraction study shown in Figure 1 (a).

The ruthenium coordination environment can be described as a slightly distorted octahedron with a Ru–Cl1 bond length (*trans* to the nitrosyl group) of 2.3418(8) Å, being significantly shorter than the Ru–Cl2 bond of 2.3664(6) Å. These features, as well as the Ru–N3 bond length of 1.742(3) Å, are in good agreement with those observed in Na$_2$[RuCl$_5$(NO)]·6H$_2$O [1.727(2) Å][44] and other related structures.[13,14] The Ru–N3–O1 angle is linear (180.0°) and the N3–O1 bond length of 1.138(4) Å is slightly shorter than in free NO (1.154 Å),[5] but markedly longer than that in free NO$^+$ (1.063 Å).[78]

XANES Spectrocopy

The results of the XANES (X-ray absorption near edge structure) experiments are presented in Figure 2. The edge energies of compounds **1**–**3**, determined as the first maximum of the first derivative (FMFD), as well as the half-height of the normalized XANES spectra (in parentheses) are 22125.7 (22124.7), 22125.2 (22123.2), and 22123.9 eV (22122.4 eV), respectively. It is clearly seen that the Ru:K edge energy for **1** is most strongly shifted towards higher energies, more than the monochromator's energy resolution of approximately 0.42 eV at 22125 eV, which indicates that the effective nuclear charge on Ru in this sample is higher than in **2** with the oxidation state 3+. The same tendency for the shift in the position of the half-height of the XANES spectra is also observed. Nonetheless, the FMFDs of **1** and **2** are similar (0.5 eV), although the difference of the corresponding half-heights is three times as large (1.5 eV). The similar shapes of the first derivative peaks of **1** and **2** may be related to the similar local geometries around the Ru ion in **1** and **2**. On the other hand, the shape of the normalized intensity of the XANES signal for **1** clearly differs from those for **2** and **3**. This seems to be
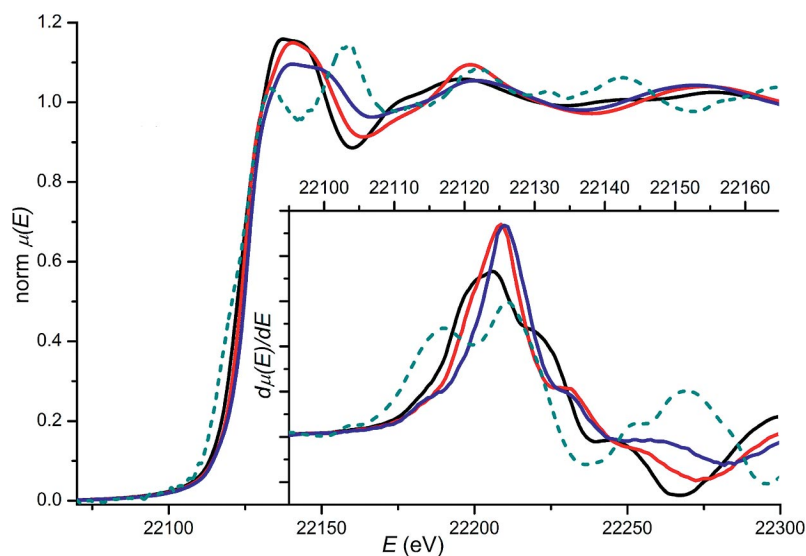

Figure 2. Ru:K edge XANES spectra together with their first derivatives (inset) for samples **3** (black line), **2** (red line), **1** (blue line), and a 0.1 μm Ru^0 metallic foil (dashed green line).

related to the fact that **2** and **3** are both coordination compounds stabilized by σ dative bonds, whereas in the case of **1**, the π back-donation in the {Ru(NO)} unit has a much stronger influence on the shape of the XANES spectra, as indicated by the broadening of the white line. The same effect of the shift of the edge energy and broadening of the white line, associated with the local environment of the investigated ion, has also been observed for {Fe(NO)}-containing systems.[49] In the literature, the edge energy of the 1s excitation (K edge) is associated with the effective charge of the photo-induced element and can also be used to determine the oxidation state, with respect to the local symmetry, in complex materials, for example, proteins. There are no reported XANES measurements for similar systems at the Ru:K edge, however, there are a number of papers on Ru-based oxides[50–52] as well as on Fe-based systems.[53,82] An energy shift per oxidation state of 1.47(12) eV can be found for Ru-based perovskites.[85] Similar values have been determined for Ru-based double perovskites,[84] Ru-based layered perovskite-like structures,[83] or ruthenium oxides.[54] Note that despite the similar energy shift per oxidation state for Ru-based compounds with different structures, these references cannot be used in an interchangeable manner. Taking into account the above remarks, the oxidation state of Ru in sample **1** can be determined by using the edge energies from the FMFDs of samples **3** and **2**, with ruthenium in the formal oxidation states of 2+ and 3+, respectively. The observed energy shift of 1.3(3) eV per oxidation state for the FMFDs of **2** and **3** results in the physical oxidation state of 3.4(3)+ for Ru in **1**. However, this value may be slightly overestimated owing to the lack of data for the Ru^{IV} reference compound. This inconvenience, together with the energy shift between Ru^{III} and Ru^{IV} of 1.3–2.5 eV presented in the literature,[85,87] suggests that, in the case of **1**, the physical oxidation state of Ru is close to 3+. Also note that **1** shows the same NO stretching vibration before and after irradiation by the 22 keV synchrotron beam at room temperature.

EXAFS Spectroscopy

The results of the EXAFS (extended X-ray absorption fine structure) experiments on compounds **1**–**3** are summarized in Figure 3. The $\chi(k)k^4$ spectra are also compared in the inset.

Analysis of the EXAFS spectrum of **3** clearly shows peaks at around 1.95 and 2.3 Å, which can be assigned to the nearest nitrogen N1 atoms of indazole and the Cl1 and Cl2 atoms, respectively. The EXAFS spectra of **1** and **2** are very similar up to 2.5 Å due to the similarities in the coordination polyhedra of the Ru ions. In **1**, the additional peak at around 2.7 Å can be attributed to the directly nonbonded Ru and O1 terminal atoms in the Ru–N3–O1 entity. The broadening of the low-R slope of the first peak of **1** (Ru–N2) at 1.5 Å is associated with overlap with the Ru–N3 scattering path, which is shorter than that of Ru–N2.

Note that the Ru–N2 distances for **3**, **2**, and **1** (1.95, 1.87, and 1.85 Å, respectively) decrease with increasing physical oxidation state of Ru. This finding can be attributed to the decrease in the ionic radius of ruthenium and is in agreement with XANES experiments and QTAIM calculations (see below).

Cyclic Voltammetry and EPR Spectroscopy

The cyclic voltammograms of ruthenium complexes **1**–**3** recorded in dmso containing 0.20 M [(nBu)$_4$N]PF$_6$ as the supporting electrolyte with a platinum wire working elec-
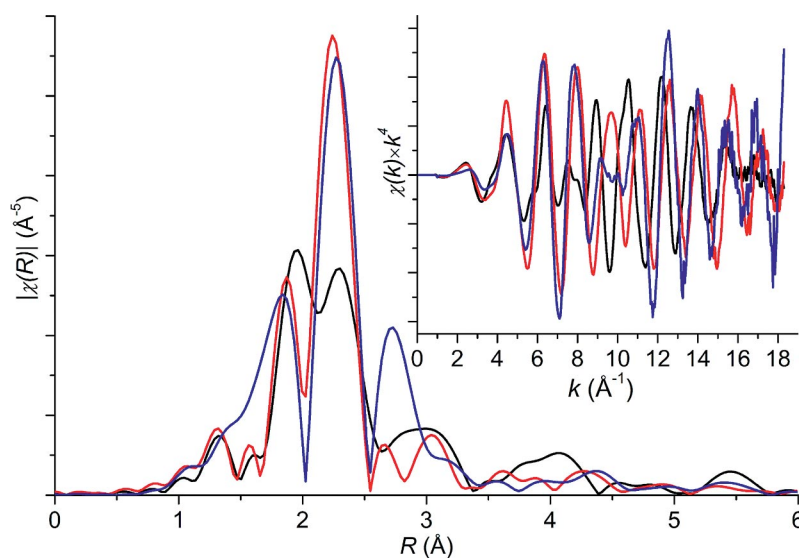

Figure 3. EXAFS $\chi(R)$ spectra for samples **3** (black line), **2** (red line), and **1** (blue line) analyzed by the Athena software with phase correction. The inset shows $\chi(k)k^4$ spectra.

trode are shown in Figure 4 (a). The electrochemical properties of **1** and **2** are comparable. Complex **1** displays one irreversible oxidation peak at 0.61 V versus Fc/Fc$^+$ and a considerably smaller irreversible reduction peak at about –1.03 V. This behavior is similar to that of **2** with ruthenium in the oxidation state 3+ (see green line in Figure 4, a). Complex **2** exhibits an oxidation wave at 0.52 V versus Fc/Fc$^+$. In strong contrast, compound **3** with ruthenium in the oxidation state 2+ shows a reversible one-electron

Figure 4. a) Cyclic voltammograms of **1** (blue line), **2** (green line), and **3** (red line: first anodic CV peak; black line: 1st and 2nd anodic CV peaks) in dmso measured at a scan rate of 100 mV s^{-1}. b) EPR spectra of **1** (blue line) and **2** (green line) in dmso at 100 K (**3** is EPR silent like **1**, spectrum not shown).

oxidation peak with $E_{1/2}$ = –0.13 V versus Fc/Fc$^+$, which corresponds to the Ru^{II}/Ru^{III} redox couple.[55] In addition, an irreversible oxidation peak can be observed at 0.47 V, very close to the first oxidation peaks observed for **1** and **2** (see black line in Figure 4, a). This observation is discussed in further detail in the theoretical section (see below). On the other hand, the EPR analysis (see Figure 4, b) shows a significant difference in the spectroscopic behavior of **1** and **2**. Compound **2** (Ru^{III}, d^5 low-spin configuration) has a typical rhombic EPR signal at 100 K due to the presence of an unpaired electron,[88] unlike **1** and **3**, which are EPR silent even at 100 K. Note that the EPR silence of **1** is due to the d^6 low-spin configuration of Ru^{II} bound to NO$^+$ (S = 0) or is a result of the antiferromagnetic or closed-shell interaction of Ru^{III} (S = ½) with NO^0 (S = ½) radical. The electronic structure of **1** will be discussed at the DFT level of theory in the computational section (see below) and compared with those of **2** and **3** in order to explain the experimental electrochemical and EPR spectroscopy results.

Electronic Structure − Localized Orbitals

Localized orbitals are unique tools for assessing the formal oxidation state of the central metal atom in coordination compounds containing innocent ligands. For example, in the case of **2** (Figure 5), one finds 3α and 2β d orbitals/electrons localized on the ruthenium(III) atom (the low-spin state), which can be considered t$_{2g}$-like d$_{xy}$, d$_{xz}$, and d$_{yz}$ orbitals if assuming an octahedral ligand-field symmetry (see the Computational Details section for the description of the Cartesian coordinate set of axes). In the case of **3**, one finds three localized doubly occupied d orbitals on ruthenium(II), which is fully in line with the formal d^6 electron configuration of Ru^{II} (see Figure 6).

The localized orbitals of **1**, which involve the t$_{2g}$-like d orbitals of ruthenium, are shown in Figure 7. In contrast to the localized d orbitals of **2** and **3**, only the d$_{xy}$ orbital of **1** is localized entirely on ruthenium (Figure 7, a), whereas the remaining two t$_{2g}$-like d orbitals of ruthenium (d$_{xz}$ and d$_{yz}$) are involved in two π bonds between ruthenium and the nitrogen atom N3 (for the atom numbering, see Figure 1, a) of the NO ligand. Such π bonds are most often interpreted as arising from π back-donation from ruthenium to the π* orbitals of NO. Very similar dative bonds have been found in the {Fe(NO)}^{6} entity.[24,26] However, there are two
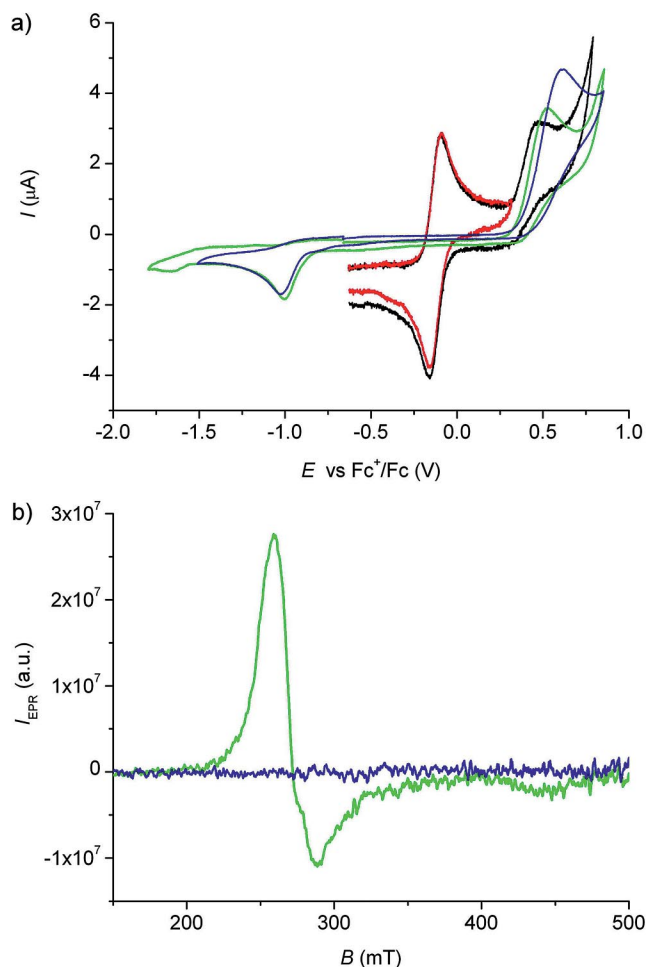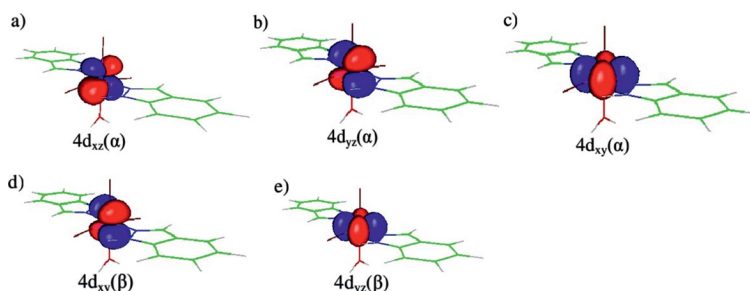

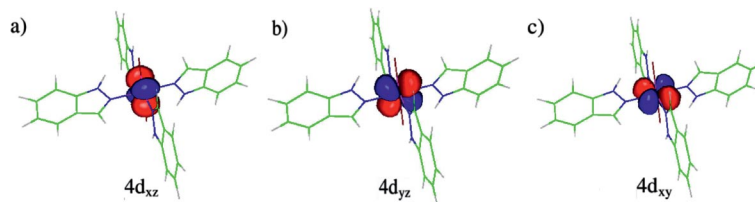Figure 5. B3LYP/ECP-DZ localized 4d orbitals of ruthenium in **2**.

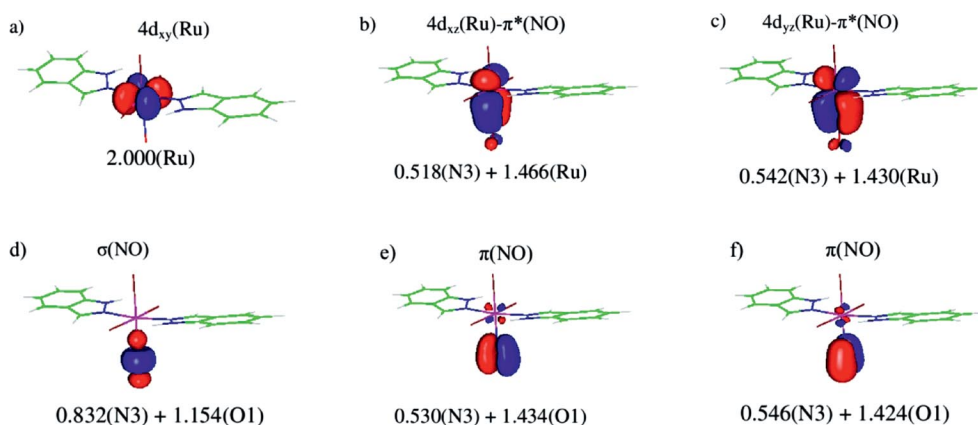Figure 6. B3LYP/ECP-DZ localized d orbitals of ruthenium in **3**.

Figure 7. B3LYP/ECP-DZ localized α d orbitals on Ru and the NO ligand of **1** and the atomic populations.

possible resonance structures available for interpreting the electron configuration of the {Ru(NO)}^{6} entity. The first is the {Ru^{II}(NO$^+$)}^{6} system[24,26,28,34] with strong π back-donation of the electron density from ruthenium to the NO ligand, which accounts for 1.06 electrons (when considering the Mulliken populations of the localized orbitals). The second resonance structure {Ru^{III}(NO^0)}^{6} implies two closely degenerate π bonds between Ru and N3, although stabiliza-

tion by antiparallel spin–spin coupling cannot be excluded by DFT calculations. A weak overlap is found between the 2s electron pair of the N3 atom and the empty d$_{z^2}$ orbital on Ru (see Figure 8, c), which represents a rather weak σ(N3–Ru) dative bond. The Cl–Ru and N2–Ru localized orbitals in **1**, which represent the σ dative bonds from the ligands towards the empty e$_g$-like orbitals of Ru (d$_{z^2}$ and d$_{x^2-y^2}$), are shown in parts a, b and d of Figure 8 and have almost the same shapes and Mulliken populations as found for **2** and **3**. In addition, none of the localized orbitals of **1** corresponds to a π bond between Ru and the Cl1, Cl2, or N2 atoms of the ligand.

In the case of **2**, in addition to the Cl1–Ru, Cl2–Ru, N2–Ru, and N4–Ru σ dative bonds (not shown), one finds three localized orbitals corresponding to a weak π donation from the p$_x$ and p$_z$ orbitals of Cl1 and Cl2, respectively, into the empty β d$_{xz}$ orbital of Ru (see Figure 8, e,f).

Electronic Structure − DAFH Analysis

The domain-averaged Fermi holes (DAFH) were used to gain an alternative insight into the electronic structure of the {Ru(NO)}^{6} entity of **1**, that is, the specification of the oxidation state of the Ru atom and the nature of its bonding with the NO ligand. Hence, the natural choice of domains in the DAFH analysis are the NO ligand and/or the central Ru atom.

In the case of the NO domain of **1** (see Figure 9), one finds nine non-zero DAFH eigenvectors, six of which have occupation numbers close to two. These represent the bonds and lone and core electron pairs that are retained in the NO domain [1s(O), 2s(O), 1s(N); σ(NO), two π(NO)].
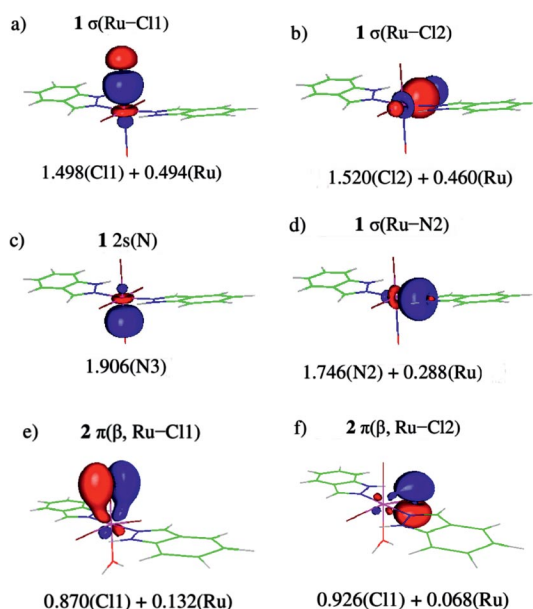

Figure 8. a–d) Localized orbitals of **1** displaying the σ bonds between Ru and Cl1, Cl2, N3, and N2 (indazole) and the atomic populations. e,f) Localized β orbitals of **2** and the atomic populations.

Some of the eigenvectors are depicted in Figure 9a [2s(O)], 9c,d [π(NO)], and 9e [σ(NO)]. The remaining three eigenvectors (with occupations of 1.736, 0.682, and 0.683, depicted in parts b,f,g of Figure 9) correspond to dangling valences of one σ and two π, formally broken, coordination bonds between Ru and the NO domains. The actual values of these occupation numbers indicate a considerable polarity of the individual components of the Ru–NO bonds. Thus, for example, in the case of the σ component of the Ru–NO bond, the occupation number of 1.732 indicates that the dominant contribution to the unevenly shared electron pair of the corresponding bond comes from N3 and the σ(Ru–NO) bond is thus Ru(+)–NO(–) polarized (i.e., the donation of the electron density from the 2s orbital of the nitrogen atom N3 into the d_{z^2} orbital of ruthenium). On the other hand, the polarization of the π components of the Ru–NO bond is in the opposite direction and the contribution of the N3 atom to the unevenly shared electron pairs of these bonds is only around 0.68 electrons. In addition, one actually obtains an almost unchanged number of nine electrons when summing the occupation numbers of all the DAFH eigenvectors of the NO domain.
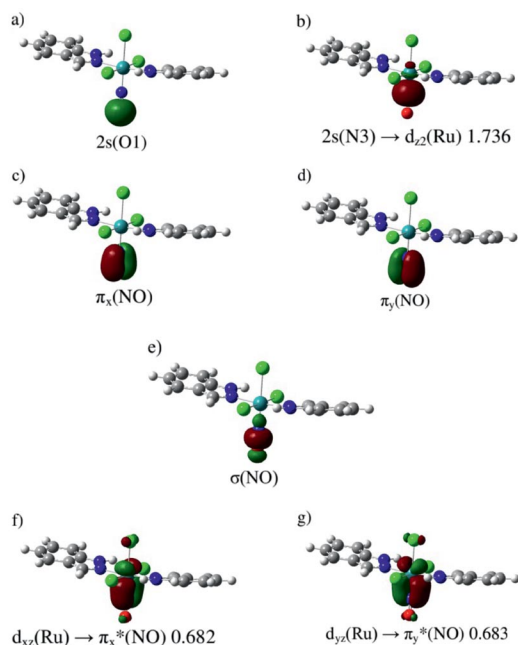

Figure 9. DAFH eigenvectors and the occupation numbers of the dangling valences of the NO domain.

The complementary contributions to unevenly shared electron pairs of the σ and π components of Ru–NO bonds straightforwardly follow from the DAFH analysis of the fragment averaged over the Ru atom domain. The corresponding eigenvectors are given in Figure 10 (a–c). Their shapes are reminiscent of the eigenvectors given in Figure 9 (e–g). This resemblance is very important as it indicates, together with the near complementarity of the corresponding occupation numbers ($1.736 + 0.226 \cong 2$; $0.68 + 1.32 \approx 2$), the shared electron-pair nature of individual components of the Ru–NO bond. In addition to three dangling valences of

individual components of the formally broken Ru–NO bond, the analysis of the Ru fragment revealed another four eigenvectors (not shown) with non-zero eigenvalues. One of the eigenvectors is close to 2.0 (the actual value is 1.838) and corresponds to the electron pair of the fully occupied d_{xy} orbital on Ru. The remaining three eigenvectors correspond to the dangling valences of formally broken dative bonds with the remaining Cl1, Cl2, and N2 atoms. Their occupation numbers are equal to 0.477, 0.401, and 0.313, respectively (the corresponding eigenvectors are not shown), and their values again indicate the Ru(+)···ligand(–) polarity of these bonds, which is in agreement with an ordinary σ dative character of the Ru–ligand bonds.
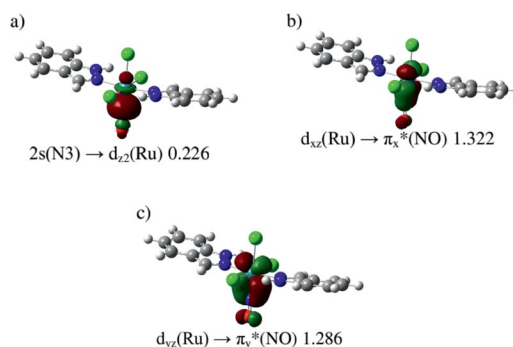

Figure 10. DAFH eigenvectors between Ru and NO for the Ru fragment in **1** and the occupation numbers on the Ru domain.

The analyses of both complementary domains (Ru and NO) provide mutually consistent pictures of the bonding, which also agree with the conclusions implied by the localized orbital analysis.

QTAIM Analysis

A meaningful assignment of the oxidation state of an atom can be obtained by comparison of the QTAIM charges in a series of molecules in which a given atom is present in well-defined oxidation states. The B3LYP/DKH2/UDZ-calculated charges on ruthenium in $RuCl_2$, $RuCl_3$, $[RuCl_5(NO)]^{2-}$, and $[RuCl_5(H_2O)]^{2-}$ are 0.98, 1.24, 1.31, and 1.23, respectively. Comparison of these data with the QTAIM charges of the studied compounds (see Table 1) shows the closest coincidence of the charge on Ru in **1** with the same charge (1.33 e) in the one-electron oxidized compound **3** (labeled as **3⁺**), which has the formal electronic configuration d^5 and the physical oxidation state 3+.

This is also in agreement with the QTAIM charges on the NO ligand atoms in **1**, which are similar to those on the NO free radical (see Table 1). The NO ligand remains strongly polarized, as in the case of the NO radical, and the total charge on the NO group/ligand is a little negative (–0.11), very different to the +1 total charge on the NO⁺ species.

In addition to the assignment of the oxidation state of the Ru atom, complementary insights into the electronic structure of the studied complex can be obtained from

Table 1. QTAIM charges calculated at the B3LYP/DKH2/UDZ level of theory.

	Ru	Cl1	Cl2	N2 (Hind)	O1	N3 (NO)
1	1.350	−0.493	−0.552	−0.708	−0.333	0.220
2	1.258	−0.447	−0.568	−0.685	−1.106	
3	1.030		−0.653	−0.685		
3⁺	1.334		−0.535	−0.715		
NO⁺					−0.152	1.152
NO					−0.398	0.398
NO⁻					−0.722	−0.278

bond critical point (BCP) electron densities, Laplacians, and ellipticities, values of which are summarized in Table 2. In particular, the BCP densities and Laplacians of the Ru–Cl1, Ru–Cl2, and Ru–N2 bonds in **1** and **2** correspond to the usual values found for σ donor bonds.[56–58] On the other hand, the Ru–N3 BCP densities and Laplacians in **1** are considerably higher and the bond is significantly shorter than Ru–N2. This is in agreement with the picture of a multiple bond between Ru and the NO ligand, which has been discussed above (see the sections Electron Structure – Localized Orbitals and DAFH Analysis). Similar BCP characteristics have been found in transition-metal carbonyl complexes in which the π back-donating character of the bonds dominates.[59–61] In the case of the NO ligand, the values of ρ_{BCP} and $\nabla^2\rho_{BCP}$ are more similar to the NO radical than to NO⁺, which is in agreement with the QTAIM charges as well as the bond lengths.

Table 2. BCP characteristics calculated at the DKH2/B3LYP/UDZ level of theory.

	d [Å]	ρ [e bohr⁻³]	$\nabla^2\rho$ [e bohr⁻⁵]	Ellipticity
1				
Ru–Cl1	2.350	0.082	0.212	0.013
Ru–Cl2	2.458	0.065	0.182	0.348
Ru–N2	2.122	0.088	0.381	0.344
Ru–N3	1.773	0.180	1.019	0.019
N3–O1	1.145	0.594	−1.757	0.001
NO⁺	1.067	0.732	−3.267	0.000
NO	1.154	0.579	−1.854	0.061
NO⁻	1.277	0.419	−0.816	0.000
2				
Ru–Cl1	2.304	0.088	0.243	0.362
Ru–Cl2	2.410	0.069	0.215	0.625
Ru–N2	2.120	0.084	0.436	0.085
Ru–O1	2.224	0.054	0.315	1.192
3				
Ru–Cl2	2.518	0.050	0.221	0.128
Ru–N2	2.115	0.082	0.460	0.070
3⁺				
Ru–Cl2	2.474	0.061	0.188	0.719
Ru–N2	2.096	0.093	0.416	0.397

The BCP ellipticities of Ru–Cl1 and Ru–N3 in **1** are close to zero, which is in agreement with the axial symmetry of these bonds. This is consistent with the σ character of the Ru–Cl1 bond. A slightly different situation is observed in the case of the Ru–N3 bond, the axial symmetry of which

originates from the contributions of one σ and two nearly equivalent π components independently detected by using localized orbitals and the DAFH analysis. The almost zero ellipticity values of the Ru–N2 bonds in **3** are consistent with σ dative bonds and weak π interactions between Ru and the ligand atoms. On the other hand, the ellipticities of the Ru–Cl2 and Ru–N2 bonds in **1** are both close to 0.35, which points towards a higher π character of the interaction between Ru and the Cl2/N2 atoms in one of the directions perpendicular to the particular bonds or confirms a π interaction in the {Ru(NO)} entity. The Ru–Cl2 bond ellipticities are considerably higher in **2** and **3⁺** (including Cl1 in **2**), which is consistent with localized orbitals from the π dative bonds of the ligands into the empty β d orbital of Ru(d⁵) in **2** as well as **3⁺** (not shown). Finally, the ellipticity of the Ru–O1 bond in **2** is greater than 1, which indicates a large polarization of the Laplacian at the BCP of this bond in one of the directions perpendicular to the bond. Very large bond ellipticities have been considered to be unstable, that is, they might easily undergo ligand exchange.[62] Nonetheless, the Laplacian eigenvalues for this bond are –0.0540, –0.0246, and 0.3937 e bohr⁻⁵. The Ru–O1 negative BCP Laplacian eigenvalues are at least an order of magnitude smaller than the eigenvalues of usual covalent bonds for which the interpretation of bond ellipticity is straightforward (this also holds for the remaining Ru–ligand bonds). B3LYP/DKH2/UDZ calculations of the [Ru(H₂O)₆]²⁺ optimized structure (D_{2h} symmetry) gives BCP ellipticities for Ru–O bonds between 0.520–0.544 for almost equal Ru–O bond lengths of 2.155 Å. On the other hand, analogous calculations on low-spin [Ru(H₂O)₆]³⁺ give three considerably different Ru–O bond ellipticities (namely 1.389, 0.813, and 0.108) for Ru–O bond lengths of 2.117, 2.042, and 2.115 Å, respectively. Although the bond ellipticities for the Ru–ligand bonds are in line with the results of the localized orbitals and DAFH analysis, they are more qualitative in meaning and have often not been considered in the analysis of metal–ligand bonds.[92–94]

The above QTAIM data can conveniently be complemented by QTAIM bond indices[63,64] (see Table 3), which give a quantitative measure of the electron exchange between atomic domains (i.e., they can be considered as a bond-order analogue). The highest values for the two-center bond index are observed for the N3–O1 and Ru–N3 bonds. This result is not surprising and straightforwardly reflects the multiple character of these bonds detected by both localized orbitals and DAFH analysis. In connection with this, it is, however, important to mention yet another aspect of Ru–NO bonding, the existence of a non-negligible bond index between the nonbonded Ru and O1 terminal atoms in the Ru–N3–O1 entity. Such a situation in which nonvanishing bond indices are observed between all pairs of atoms in the array is typical for multicenter bonding,[65–67] which is reflected in the non-negligible value of the three-center bond index in the Ru–N3–O1 entity. The negative sign of this index is typical for three-center–two-electron (3c–2e) bonding.[68–70,99,100] This result, together with the axial symmetry of the bonds in the array (indicated

by the negligible ellipticity of the Ru–N3 and N3–O1 bonds), clearly implies that the bonding in the Ru–N3–O1 unit involves two 3c–2e bonds of π symmetry formed by the overlap of the d–p–p orbitals on individual atoms in the array. The remaining bond indices for Ru–Cl1, Ru–Cl2, and Ru–N2 indicate that the corresponding bonds have the character of simple σ dative bonds.

Table 3. QTAIM bond pair indices in **1** calculated at the B3LYP/DKH2/UDZ level of theory.

Two center	Bond-pair index
Ru–Cl1	0.762
Ru–Cl2	0.708
Ru–N2	0.598
Ru–N3	1.554
Ru–O1	0.492
N3–O1	1.976
Three center	
Ru–N3–O1	–0.398

Mulliken Population Analysis of the d Orbitals of Ru

The electronic configuration of the Ru central atom can be described within the quasi-octahedral approximation of the coordination polyhedron with a straightforward t_{2g}/e_g-like assignment of the individual d-orbital populations (see Table 4). To avoid any additional problems of the MPA with diffuse functions for the UDZ basis set, the B3LYP/ECP-DZ/PCM(dmso) d-orbital populations will be presented (nonetheless, in the case of uncontracted basis sets, the difficulties associated with diffuse functions seem to be much less pronounced and MPA in the UDZ basis set seems to be robust). Total Mulliken d-electron populations calculated at the B3LYP/ECP-DZ/PCM(dmso) level are similar for **1**–**3** (the total d-electron populations are 6.54, 6.62, 6.63, and 6.39 electrons for $[RuCl_5(NO)]^{2-}$, $[Ru^{III}Cl_5(H_2O)]^{2-}$, $Ru^{II}Cl_2$, and $Ru^{III}Cl_3$, respectively). Hence, the differences in the populations between the compounds with ruthenium in the oxidation states 2+ and 3+ vary between 0.1 and 0.3 electrons.

Table 4. ECP-DZ Mulliken d-orbital populations on ruthenium in **1**–**3** and **3⁺**.

Comp.	Orbitals	d_{z^2}	d_{xz}	d_{yz}	$d_{x^2-y^2}$	d_{xy}	t_{2g}	Total[a]
1	α+β	0.80	1.47	1.52	0.76	2.00	4.99	6.56
2	α	0.37	1.01	0.98	0.35	1.00	2.99	6.58
	β	0.34	0.29	0.92	0.32	0.99	2.21	
3	α+β	0.53	1.98	1.98	0.50	1.80	5.75	6.78
3⁺	α	0.33	1.00	0.96	0.35	0.35	2.96	6.50
	β	0.31	0.99	0.23	0.32	0.32	2.22	

[a] Total d population, that is, α + β.

It seems that the t_{2g}-like d-electron population might be more suitable for characterization of the oxidation state than the total d-electron population (see Table 4). In this respect, the t_{2g}-like d-electron populations (d_{xy}, d_{xz}, d_{yz}) of **1** and **2** account for 4.99 and 5.20 electrons, respectively. In the case of **2**, the low population of the β d_{xz}(Ru) atomic orbital indicates an open d-subshell of Ru; the non-zero d population comes from Cl2→Ru π donation. By neglecting the d population of the β d_{xz} orbital we obtain the t_{2g} population of 4.91 electrons for **2**. On the other hand, the t_{2g} orbitals of **3** are populated by 5.75 electrons. The d_{xy} population of **3** is 1.80 and indicates the π back-donation of electron density into p orbitals of ligand atoms, although some artifact of the MPA as well as small deviations between the orientation of the Cartesian axes and the coordination polyhedra might also contribute. The d_{xz} and d_{yz} electron populations of **1** are both close to 1.50 and in agreement with the two π(Ru–N3)-localized orbitals or DAFH eigenvectors found. The populations of the e_g d orbitals (d_{z^2} and $d_{x^2-y^2}$) of **1** and **2** are also very similar and arise from σ dative bonds between the ligands and ruthenium.

The total d-electron populations indicate only qualitatively the oxidation state of the ruthenium atoms in **1**–**3**. On the other hand, the t_{2g}-like d populations yield physical t_{2g} d-electron populations on Ru close to five in **1** and **2** and therefore the physical oxidation state of Ru in **1** is 3+. Furthermore, the MPA charge on the NO ligand in **1** is close to zero (or slightly negative), which also agrees with the physical electronic structure $\{Ru^{III}(NO)^0\}$. The MPA of NO is not considered in further detail.

Redox Behavior

The HOMO and LUMO orbitals are very useful indicators of the redox behavior for a given species. As the cyclic voltammetry experiments show, the species **1**, **2**, and **3⁺** are oxidized at very similar potentials, and thus the shapes of their HOMO orbitals should be similar. Nonetheless, as can be seen in Figure 11, the HOMO of **1** is localized on the indazole rings, whereas the HOMO of **2** has Ru–Cl1 antibonding character (both α and β spin orbitals). Unlike **1** and **2**, the HOMO orbitals of **1** and **3⁺** (Figure 11) have the same shape. This is in agreement with the same redox behavior of **1** and **3⁺** observed in the cyclic voltammetry experiments.

The discrepancy between the similar oxidation behavior of **1** and **2** and the differently shaped HOMO orbitals of **1** and **2** is worth considering. In the HOMO–1 or HOMO–2 orbitals of **2**, a non-negligible part of the electron density is localized on the indazole rings (see Figure 12b for the α HOMO–1 orbital of **2**). The HOMO orbitals exactly fit with the X-ray structures of **1** and **2** and have an antibonding character between Ru and Cl2 (the HOMO−4 of the reoptimized geometry of **1**, not shown). During the geometry optimization of **1** and **2**, the indazole rings relax towards the Cl2–Ru–N2 plane and the Cl2–Ru–N2–N1 dihedral
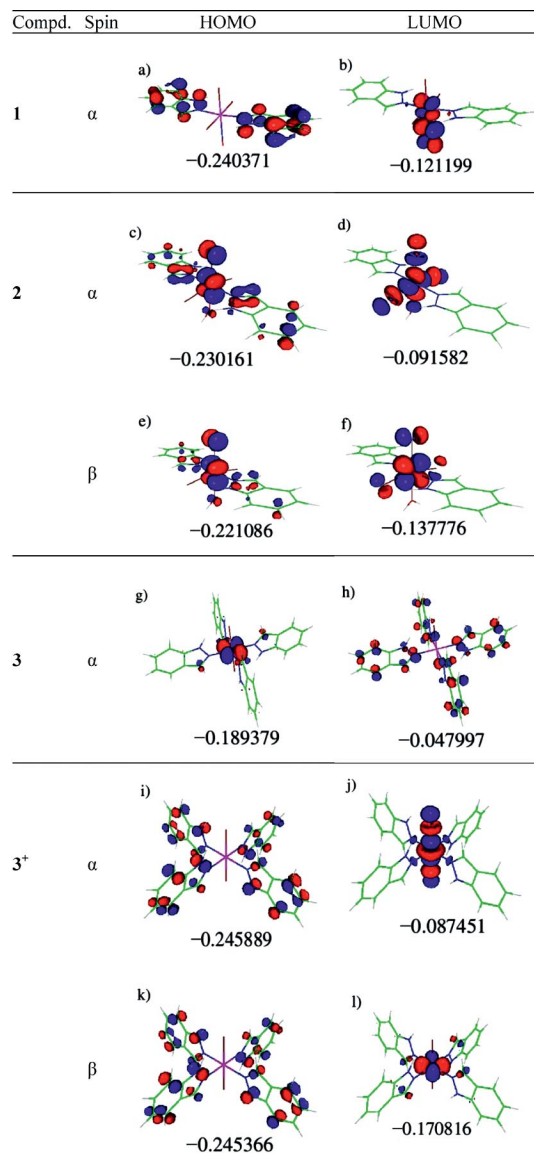
Figure 11. B3LYP/ECP-DZ/PCM(dmso)-calculated HOMO and LUMO orbitals and the corresponding eigenvalues (in hartrees) for **1**–**3** and **3+**.

Figure 12. B3LYP/ECP-DZ/PCM(dmso)-calculated α(LUMO+1) and α(HOMO–1) frontier orbitals and the corresponding eigenvalues (in hartrees) for **1** and **2**, respectively.

which is in agreement with the reversible cyclic voltammetry oxidation peak observed for **3**.

CASSCF

Although the DFT method has been used to elucidate the electronic structures of the studied compounds, with the focus on the {Ru(NO)}^{6} entity of **1**, the contribution from antiparallel spin–spin coupling is worth considering by means of CASSCF calculations. The broken-symmetry DFT calculations did not converge, probably because of the very short distance between the two spin centers (Ru, NO). The open-shell DFT calculation on **1** gives a triplet spin state that is energetically less stable than the singlet spin state, and a spin population of 1.8 is found on Ru, whereas the nitrogen and oxygen atoms of NO both have a spin population close to –0.25. In addition, no difference in total energy is found for the UKS/RKS B3LYP calculations on **1** in the singlet spin state, which does not indicate any antiparallel spin–spin coupling.

The CASSCF calculation started with six active electrons from the B3LYP/ECP-DZ t_{2g} localized orbitals [d_{xy}(Ru), d_{xz}(Ru)–π*(NO), d_{yz}(Ru)–π*(NO); see Figure 7, a–c] and the canonical LUMO and LUMO+1 B3LYP/ECP-DZ orbitals (see part b of Figure 11 and Figure 12, a) have been included in the virtual active space (i.e., six electrons in five orbitals). The final CASSCF natural orbitals are shown in Figure 13. The active orbital occupation numbers (0, 1, 2) in the individual state determinants are ordered according to the labels in Figure 13 (i.e., [abcde]). The ground-state CASSCF wavefunction has a dominant (87.3 %) contribution from the ground-state [22200] determinant, whereas the excited determinants [21111], [22020], and [20202] have weights of 5.1, 3.2, and 3.0 %, respectively. The ground state has a negligible contribution from the [22110] and/or [21201] determinants, and the antiparallel spin–spin coupling comes predominantly from the [21111] determinant, the weight of which points to a small antiferromagnetic interaction in the {Ru(NO)}^{6} entity.

angles for **1** and **2** change from around 45° to almost 0°, which causes reordering of the frontier orbitals. In addition, the interaction of the Cl2 ligands with the H atoms of the water molecule in the case of **2** need not be properly described at the DFT/B3LYP/PCM(dmso) level of theory. The inappropriate description of the interaction of Cl2 atoms with the hydrogen atoms of the water ligand leads to further changes in the optimized geometry of **2**, which causes additional reordering of the frontier orbitals in **2**. This might also contribute to the large ellipticity of the Ru–O1 bond in **2**. On the other hand, our DFT-optimized structure should better correspond to the structure in solution, which might differ significantly from the solid-state structure.

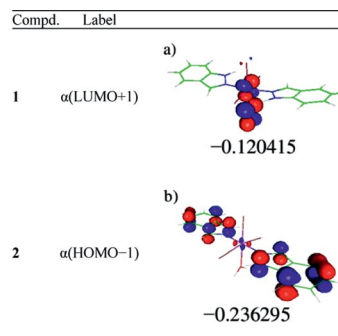The HOMO of **3** (Figure 11) is presumably localized on Ru and the β LUMO of **3+** is the same as the HOMO of **3**,

a)

-0.521124 (2.000)

b)

-0.441965 (1.872)

c)

-0.440005 (1.868)

d)

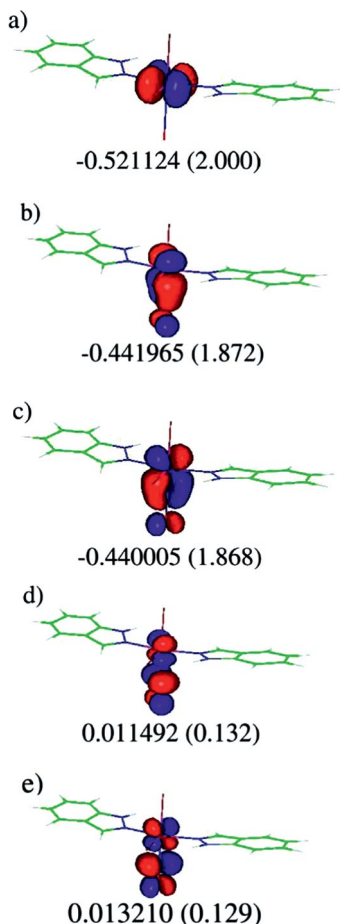0.011492 (0.132)

e)

0.013210 (0.129)

Figure 13. CASSCF/ECP-DZ natural orbitals of **1**. Eigenvalues are given in hartrees (ground-state CASSCF occupation numbers).

Conclusions

Our DFT calculations have confirmed that the bonding in the $\{Ru(NO)\}^6$ entity is due to one rather weak σ dative bond and two strong π back-donating bonds. This is implied by both the localized orbitals and DAFH analysis. In addition, the CASSCF calculation confirmed that the $\{Ru(NO)\}^6$ entity has a predominantly closed-shell character. The two π bonds are thus interpreted as being Ru–NO back-dative bonds,[34] as in analogous $\{Fe(NO)\}^6$ species,[24,26] which leads to the $\{Ru^{II}(NO)^0\}^6$ formal electronic structure. The closed-shell interaction in **1** was also confirmed by EPR spectroscopy and magnetic susceptibility data. Nonetheless, as indicated by the atomic populations of the localized orbitals, almost 1.1 electrons are transferred by the π back-donation from ruthenium to the π*(NO) orbitals. This is also in agreement with the QTAIM charges as well as Mulliken d populations (especially when considering the t_{2g} d populations), which provide evidence for the physical oxidation state 3+ of Ru in **1**. The BCP characteristics of the Ru–N3 and N3–O1 bonds are also indicative of Ru^{III} as the physical oxidation state and a neutral NO ligand. The BCP electron density and the Laplacian of the N–O bond in the coordinated nitrosyl ligand are closer to the NO radical than to NO$^+$, and the same is implied by

the NO ligand QTAIM charges. These theoretical findings are supported by the XANES experiment, which suggests the physical oxidation state of Ru to be higher than 3+. Nonetheless, the enhanced d–p interaction in the $\{Ru(NO)\}^6$ entity is manifested by the different shapes of the XANES spectra of **1** and **2**, although the corresponding first derivatives, which are more related to the oxidation state, are very similar. In addition, the cyclic voltammetry experiments showed that compounds **1**, **2**, and **3$^+$** have similar oxidation waves. However, a straightforward assignment of the oxidation process by cyclic voltammetry was not possible; the oxidation may be ruthenium- as well as ligand-centered. The B3LYP HOMO orbitals of **1** and **3$^+$** are in agreement with each other and both are ligand (indazole)-centered, whereas the HOMO of **2** is the Ru–Cl1 antibonding orbital. Note that the HOMO–1 of **2** is also ligand-centered. It seems that the interactions of Cl2 atom(s) with the H atoms of the water ligand are not properly described by the B3LYP functional, which affects the reoptimized geometry of **2** as well as the order of the frontier orbitals. Nonetheless, taking into account the experimental results (redox behavior, IR spectra, and XANES/EXAFS data) and the theoretical investigations (atomic charges and populations), we can assign the physical electronic structure to a closed-shell $\{Ru^{III}(NO)^0\}^6$ configuration.[25,29]

The (nonmeasurable) formal configuration of $\{Ru^{II}(NO)^+\}^6$ is physically better described as $\{Ru^{III}(NO^0)\}^6$, which provides another example of the discrepancy between formal and physical oxidation states in metal complexes.[23,28,34]

Experimental Section

Materials: The starting compound *mer,trans*-[RuCl$_3$(H$_2$O)(Hind)$_2$] was prepared according to a literature protocol.[5] NaNO$_2$, FeSO$_4$, and 1*H*-indazole were purchased from Aldrich, and RuCl$_3$·nH$_2$O and Na^{15}NO$_2$ were obtained from Johnson-Matthey and Eurisotop, respectively. NO gas was generated by the dropwise addition of a 40% aqueous solution of NaNO$_2$ to a 20% aqueous solution of FeSO$_4$ containing the same volume of concentrated HCl.

Synthesis of *mer,trans*-[RuCl$_3$(Hind)$_2$(NO)] (1)

Method a: A stream of NO gas was passed through a solution of *mer,trans*-[RuCl$_3$(H$_2$O)(Hind)$_2$] (100 mg, 0.2 mmol) in acetone (20 mL) for 10 min. The color of the solution changed from orange to ruby. The solution was filtered and allowed to crystallize in a closed vessel. After 72 h, the dark-red crystals were filtered off, washed with acetone, and dried in air, yield 65 mg (63%). The crystals were readily soluble in dmso and dmf, moderately soluble in acetonitrile, and insoluble in methanol, 2-propanol, dichloromethane, thf, and water. ^{1}H NMR (500 MHz, [D$_6$]dmso): δ = 13.77 (s, 2 H, 1-H), 8.80 (s, 2 H, 3-H), 7.99 (d, *J* = 8.31 Hz, 2 H, 4-H), 7.80 (d, *J* = 8.60 Hz, 2 H, 7-H), 7.58 (t, *J* = 8.38 Hz, 2 H, 6-H), 7.31 ppm (t, *J* = 7.83 Hz, 2 H, 5-H). ^{13}C NMR (125 MHz, [D$_6$]dmso): δ = 141.51, 139.32, 129.77, 122.80, 122.01, 121.76, 111.58 ppm. ^{15}N NMR (50 MHz, [D$_6$]dmso): δ = 165.04 (NH) ppm. IR (ATR): ṽ = 3344 (NH), 1870 (NO), 1627 (C=N), 1513, 1360, 1239, 1088, 854, 837, 750 cm^{-1}. UV/Vis (dmso): λ_{max} (ε) = 507 (81), 279 nm (13110 M^{-1} cm^{-1}). MS (ESI, positive ion mode,

acetone): m/z = 496 $[M + Na]^+$. $C_{14}H_{12}Cl_3N_5ORu$ (473.71): C 35.50, H 14.78, N 2.55; found C 35.79, H 14.58, N 2.41.

$[RuCl_3(^{15}NO)(Hind)_2]$ was produced as above by using $Na^{15}NO_2$. IR (ATR): $\tilde{\nu}$ = 3343 (NH), 1832 (NO), 1625 (C=N) cm^{-1}. ^{15}N NMR (50 MHz, $[D_6]dmso$): δ = 316.23 ppm.

Method b

$Na_2[RuCl_5(NO)]\cdot 6H_2O$: $RuCl_3\cdot 3H_2O$ (2.50 g, 9.5 mmol) was dissolved in degassed 1 M hydrochloric acid and heated at reflux for 10 min. A solution of $NaNO_2$ (1.97 g, 28.5 mmol) in water (5 mL) was then added dropwise over 10–12 min. The resulting brown solution was heated at reflux for 3.5 h under argon and the solvent was evaporated on a steam bath. The residue was dissolved in ethanol (12 mL) and the dark-red solution filtered. Needle-like crystals were formed after 3–4 h. The crystals were separated by filtration and the filtrate evaporated to dryness on a steam bath. The residue (2.0 g) was dissolved in 6 M HCl (5 mL) and allowed to stand at room temperature. The resulting red crystals, which were suitable for X-ray data collection, were filtered off, washed with a small amount of cold ethanol, and dried in air, yield 1.8 g. $H_{12}Cl_5Na_2NO_7Ru$ (462.41): calcd. N 3.03; found 3.32. The X-ray diffraction structure of this compound was identical with that reported previously.[71]

$(H_2ind)_2[RuCl_5(NO)]$: $(H_2ind)_2[RuCl_5(NO)]$ was crystallized from a solution prepared by the reaction of $Na_2[RuCl_5(NO)]\cdot 6H_2O$ (0.5 g, 1.1 mmol) in 6 M HCl (2 mL) with excess indazole (2.0 g, 17.1 mmol) in 6 M HCl (14 mL) at 5 °C, yield 623 mg (74%).

$mer,trans$-$[RuCl_3(NO)(Hind)_2]$: $(H_2ind)_2[RuCl_5(NO)]$ (100 mg, 0.18 mmol) was heated in an evacuated glass oven at 180 °C for 16 h to form a pale-violet product, yield 82 mg, 96%. The IR spectrum was identical to that for the sample obtained by method a.

Physical Measurements: Elemental analyses were performed by the Microanalytical Service of the Faculty of Chemistry of the University of Vienna on a Perkin–Elmer 2400 CHN Elemental Analyzer. NIR spectra were measured with a Perkin–Elmer 370 FTIR 2000 spectrometer (4000–400 cm^{-1}) equipped with an ATR unit. UV/Vis spectra were recorded with a Perkin–Elmer Lambda 20 UV/Vis spectrophotometer using samples dissolved in dmso. Electrospray ionization mass spectrometry was carried out with a Bruker Esquire 3000 spectrometer (Bruker Daltonics, Bremen, Germany) with acetone as solvent. Expected and measured isotope distributions were compared. The electrochemical measurements were performed with a HEKA PG 284 (Lambrecht, Germany) potentiostat/galvanostat using the PotPulse 8.53[104] software package. All cyclovoltammetric experiments were performed at room temperature under nitrogen. Platinum wires were used for the working and counter electrodes, and a silver wire was used as the pseudoreference electrode. The recorded voltammetric curves were obtained at a scan rate of 0.1 Vs^{-1}. Sample solutions were prepared with a concentration of 0.5 mM in dmso with 0.2 M TBAPF$_6$ as supporting electrolyte and purged with N_2 for 5 min before each experiment. Ferrocene (Fc) was used as an internal standard. The ^1H, ^{13}C, and ^{15}N NMR spectra were recorded at 500, 125, and 50 MHz with a Bruker Avance III 500 MHz (Ultrashield Magnet) spectrometer in $[D_6]dmso$. 2D $^{13}C,^1H$ HSQC, $^{15}N,^1H$ HSQC, $^{13}C,^1H$ HMBC, and $^1H,^1H$ COSY experiments were performed on 1. The solvent residual peak for ^1H and ^{13}C was used as internal reference, whereas ^{15}N chemical shifts are given relative to external NH_4Cl. The EPR spectra were recorded with an EMX EPR spectrometer (Bruker, Germany) at 100 K by using liquid nitrogen. Magnetic data were obtained with a Quantum Design MPMS SQUID susceptometer. Magnetic susceptibility measurements were performed in the 2–

300 K temperature range under a 0.5 T applied magnetic field and diamagnetic corrections were applied by using Pascal's constants.

X-ray Crystallography: X-ray diffraction was performed with a Bruker X8 APEXII CCD diffractometer at 100 K. A single crystal was placed 40 mm from the detector and 1653 frames were measured, each for 30 s over 1° scan width. The data were processed by using the SAINT software.[72] The structure was solved by direct methods and refined by full-matrix least-squares techniques. Non-hydrogen atoms were refined with anisotropic displacement parameters. H atoms were placed at calculated positions and refined as riding atoms in the subsequent least-squares refinements. The isotropic thermal parameters were estimated to be 1.2 times the values of the equivalent isotropic thermal parameters of the non-hydrogen atoms to which hydrogen atoms are bonded. The following computer programs and equipment were used: SHELXS-97, SHELXL-98,[73] SCHAKAL,[74] and an Intel CoreDuo personal computer. Crystal data, data collection parameters, and structure refinement details for **1** are given in Table 5.

Table 5. Crystal data and details of data collection for **1**.

Empirical formula	$C_{14}H_{12}Cl_3N_5ORu$
M_r	473.71
Space group	$C2/c$
a [Å]	14.6560(6)
b [Å]	12.2121(6)
c [Å]	9.6281(4)
β [°]	104.829(4)
V [Å^3]	1665.85(13)
Z	4
λ [Å]	0.71073
$\rho_{calcd.}$ [g cm^{-3}]	1.889
Crystal size [mm]	$0.25 \times 0.08 \times 0.05$
T [K]	100(2)
μ [mm^{-1}]	1.434
R_1[a]	0.0230
wR_2[b]	0.0515
GOF[c]	1.090

[a] $R_1 = \Sigma ||F_o| - |F_c||/\Sigma|F_o|$. [b] $wR_2 = \{\Sigma[w(F_o^2 - F_c^2)^2]/\Sigma[w(F_o^2)^2]\}^{1/2}$. [c] GOF = $\{\Sigma[w(F_o^2 - F_c^2)^2]/(n - p)\}^{1/2}$, in which n is the number of reflections and p is the total number of parameters refined.

X-ray Absorption Spectroscopy: X-ray absorption spectroscopy (XAS) experiments were performed at the beamline X1 at DORIS III in Hasylab, DESY, Hamburg, Germany. The spectra were collected in transmission mode at room temperature at the same time as the energy shift reference (20 μm Rh foil). The double-crystal Si(311) monochromator ($\Delta E/E = 1.9 \times 10^{-5}$) was calibrated to the edge energy of 22117.0 eV of a 0.1 μm Ru metallic foil. Samples were diluted in cellulose and measured as pellets. The data were analyzed by using the Athena software.[75,76] The Ru:K edges of samples **1**–**3** were measured.

Computational Details: Unless otherwise stated, the B3LYP functional[77] was used for geometry optimizations starting from the X-ray structures and single-point calculations in dmso solutions by using the integral equation formalism version of the polarized continuum model (PCM).[78] Compounds **1** and **3** in the singlet spin state (closed shell) as well as compounds **2** and **3$^+$** (the one-electron oxidized compound **3**) in the doublet spin state (open shell) were investigated. The LANL(28)[79] effective core potential and LANL08[80] basis set were used for the Ru atom, and the remaining atoms were treated by using the cc-pVDZ basis sets[81,82] (abbreviated as ECP-DZ). The presented frontier orbitals and localized or-

2516

bitals (using the Pipek–Mezey procedure) were obtained by using the same ECP-DZ basis sets. On the other hand, the DAFH analysis, which utilizes the QTAIM approach, has been performed at the scalar second-order Douglas–Kroll–Hess (DKH2)[83–87] level of theory. Uncontracted basis sets of DZ (abbreviated as UDZ) quality were employed in the DKH2 calculations, that is, Dyall's UDZ basis set (21s14p10d1f)[88] was used for the ruthenium atom, whereas Dunning's uncontracted cc-pVDZ basis sets[54,55] were used for the Cl, O, N, and C atoms and the uncontracted 6-31G basis set[89] for the hydrogen atoms. The Gaussian 03 software[90] was used for all DKH2 and ECP calculations. For description purposes, the Ru–Cl2, Ru–N2, and Ru–Cl1 (Ru–N4 for compound **3**) bonds are (nearly) coincident with the x, y, and z Cartesian axes, respectively (for the atom numbering, see Figure 1). The DAFH analysis was performed with the WinBader program,[91] and the QTAIM analysis with the AIMAll software.[92]

The B3LYP/ECP-DZ localized and frontier canonical orbitals were obtained by using the ORCA software.[93,94] In addition, the ORCA package was used to determine the Mulliken populations of the localized and canonical orbitals. All the orbitals (as well as the DAFH eigenvectors) are drawn with isovalues of 0.05 e bohr^{-3}. The gOpenMol program[95] was used to plot the localized and canonical orbitals, and the DAFH eigenvectors were visualized by GaussView software.[96]

The CASSCF calculation of **1** in the B3LYP/ECP-DZ/PCM(dmso)-optimized geometry was also performed with the ORCA package. The minimal active space, used to elucidate the antiferromagnetic interaction in the {Ru(NO)}^{6} entity, accounted for the t_{2g} d electrons of Ru and the π*(NO) orbitals.[97] The starting active space was built up of the localized B3LYP/ECP-DZ t_{2g}-like d orbitals of Ru [d_{xy}(Ru), d_{xz}(Ru)–π*(NO), d_{yz}(Ru)–π*(NO)] and the LUMO and LUMO+1 canonical B3LYP/ECP-DZ orbitals (in total six electrons in five orbitals). For further details see the CASSCF section. A state-averaged CASSCF calculation for the five lowest roots was performed and the CASSCF single-root calculation was then restarted from the obtained state-averaged natural orbitals.

Several different theoretical methods were employed to reveal the electronic structures of the studied compounds. The localized orbitals are a useful tool for elucidating electronic structures, providing essential information about the shapes and types of bonds between atoms as well as about the lone pairs and core parts of atoms.

Quantum Theory of Atoms-in-Molecules (QTAIM) analysis is based on the topological analysis of electron density $\rho(r)$,[42,43] which results in partitioning of the electron density into domains associated with individual atoms. The integration of the electron density within the individual domains provides the QTAIM atomic charges. A similar integration can also be applied to the straightforward extension of the concept of bond indices as quantitative measures of electron-sharing between individual atoms. Further information can be extracted from bond characteristics such as electron density ρ, its Laplacian $\nabla^2\rho$, and bond ellipticity ε at bond critical points (BCP) defined by Equations (1) and (2) in which $\lambda_1 < \lambda_2 < 0 < \lambda_3$ are the eigenvalues of the Hessian of the BCP electron density. BCP is the bond path point with the minimal electron density.

$$\nabla^2\rho = \lambda_1 + \lambda_2 + \lambda_3 \tag{1}$$

$$\varepsilon = \frac{\lambda_1}{\lambda_2} - 1 \tag{2}$$

Domain-averaged Fermi hole (DAFH) analysis was proposed to extract highly visual information about the electronic structure or bonding, especially in molecules with nontrivial bonding patterns.[98–103] Its principles are described in the original literature.[39–41] Especially interesting and chemically relevant information can be extracted from the holes defined by atomic domains resulting from Bader or Mulliken analysis, but more complex domains, formed by the union of several atomic domains, which correspond, for example, to certain functional groups or interesting molecular fragments, can be analyzed as well. In any case, the holes provide information about the electron pairs (chemical bonds, core and valence lone pairs) retained in the domain and about the broken or dangling valences resulting from the formal splitting of the bonds required for the isolation of the corresponding fragments from the rest of the molecule. The structural information is retrieved from the combination of qualitative insights provided by the visual inspection of individual DAFH eigenvectors and their eigenvalues (occupation numbers). Occupation numbers close to two typically correspond to electron pairs (chemical bonds, core and/or valence lone pairs) that are retained in the analyzed domain. Occupation numbers that considerably deviate from the ideal value of two usually denote the dangling valences of the formally broken bonds and the actual values provide information about the polarity of these bonds.

In connection with the above broad spectrum of independent theoretical tools and procedures used, it is extremely important and worthy that the picture of the bonding provided by all of them is very similar and mutually consistent.

Supporting Information (see footnote on the first page of this article): ^{1}H and ^{13}C NMR spectra of **1** and ^{15}N NMR of ^{15}NO-labeled **1**, ^{15}N,^{1}H HSQC, ^{1}H,^{1}H COSY, and ^{13}C–^{1}H HMBC plots for **1**, and optimized geometries of **1**–**3** and **3$^+$** (including full details of Gaussian 03 calculations).

Acknowledgments

[1] a) W. H. Ang, P. J. Dyson, *Eur. J. Inorg. Chem.* **2006**, *20*, 4003–4018; b) W. H. Ang, E. Daldini, R. Scopelliti, L. Juillerat-Jeannerat, P. J. Dyson, *Inorg. Chem.* **2006**, *45*, 9006–9013; c) C. Gossens, A. Dorcier, P. J. Dyson, U. Rothlisberger, *Organometallics* **2007**, *26*, 3965–3975; d) P. J. Dyson, G. Sava, *Dalton Trans.* **2006**, 1929–1933.

[2] a) C. G. Hartinger, S. Zorbas-Seifried, M. A. Jakupec, B. Kynast, H. Zorbas, B. K. Keppler, *J. Inorg. Biochem.* **2006**, *100*, 891–904; b) P. Heffeter, K. Böck, B. Atil, M. A. Reza Hoda, W. Körner, C. Bartel, U. Jungwirth, B. K. Keppler, M. Micksche, W. Berger, G. Koellensperger, *J. Biol. Inorg. Chem.* **2010**, *15*, 737–748.

[3] a) J. M. Rademaker-Lakhai, D. van den Bongard, D. Pluim, J. H. Beijnen, J. H. M. Schellens, *Clin. Cancer Res.* **2004**, *10*, 3717–3727; b) E. Alessio, G. Mestroni, B. Bergamo, G. Sava, *Curr. Top. Med. Chem.* **2004**, *4*, 1525–1535.

[4] M. R. Berger, F. T. Garzon, B. K. Keppler, D. Schmähl, *Anticancer Res.* **1989**, *9*, 761–765.

[5] B. Cebrián-Losantos, E. Reisner, C. R. Kowol, A. Roller, S. Shova, V. B. Arion, B. K. Keppler, *Inorg. Chem.* **2008**, *47*, 6513–6523.

[6] B. Serli, E. Zangrado, E. Iengo, G. Mestroni, L. Yellowlees, E. Alessio, *Inorg. Chem.* **2002**, *41*, 4033–4043.

[7] B. Serli, E. Zangrado, T. Gianferrara, L. Yellowlees, E. Alessio, *Coord. Chem. Rev.* **2003**, *245*, 73–83.

[8] A. Vacca, M. Bruno, A. Boccarelli, M. Coluccia, D. Ribatti, A. Bergamo, S. Garbisa, L. Sartor, G. Sava, *Brit. J. Cancer* **2002**, *86*, 993–998.

[9] L. Morbidelli, S. Donnini, S. Filippo, L. Messori, F. Piccioli, P. Orioli, G. Sava, M. Ziche, *Brit. J. Cancer* **2003**, *88*, 1484–1491.

[10] R. B. Silverman, *Acc. Chem. Res.* **2009**, *42*, 439–445.

[11] A. de Mel, F. Murad, A. M. Seifalian, *Chem. Rev.* **2011**, *111*, 5742–5767.

[12] R. F. Furchgott, *Angew. Chem.* **1999**, *111*, 1990; *Angew. Chem. Int. Ed.* **1999**, *38*, 1870–1880.

[13] J. Garthwaite, S. L. Charles, R. Chess-Williams, *Nature* **1988**, *336*, 385–388.

[14] T. M. Dawson, S. H. Snyder, *J. Neurosci.* **1994**, *14*, 5147–5159.

[15] G. Cirino, E. Distrutti, J. L. Wallace, *Inflammation Allergy: Drug Targets* **2006**, *5*, 115–119.

[16] F. S. Laroux, K. P. Pavlick, I. N. Hines, S. Kawachi, H. Harada, S. Bharwani, J. M. Hoffman, M. B. Grisham, *Acta Phys. Scand.* **2001**, *173*, 113–118.

[17] G. A. Blaise, D. Gauvin, M. Gangal, S. Authier, *Toxicology* **2005**, *208*, 177–192.

[18] A. Weigert, B. Brüne, *Nitric Oxide* **2008**, *19*, 95–102.

[19] B. Brüne, A. von Knethen, K. B. Sandau, *Cell Death Differ.* **1999**, *6*, 969–975.

[20] C. K. Jørgensen, *Coord. Chem. Rev.* **1966**, *1*, 164–178.

[21] W. Kaim, *Eur. J. Inorg. Chem.* **2012**, 343–348.

[22] J. H. Enemark, R. D. Feltham, *Coord. Chem. Rev.* **1974**, *13*, 339–406.

[23] P. Chaudhuri, C. N. Verani, E. Bill, E. Bothe, T. Weyhermuller, K. Wieghardt, *J. Am. Chem. Soc.* **2001**, *123*, 2213–2223.

[24] M. Li, D. Bonnet, E. Bill, F. Neese, T. Weyhermuller, N. Blum, D. Sellmann, K. Wieghardt, *Inorg. Chem.* **2002**, *41*, 3444–3456.

[25] O. V. Sizova, V. I. Baranovski, N. V. Ivanova, V. V. Sizov, *Mol. Phys.* **2003**, *101*, 715–720.

[26] G. R. Serres, C. A. Grapperhaus, E. Bothe, E. Bill, T. Weyhermuller, F. Neese, K. Wieghardt, *J. Am. Chem. Soc.* **2004**, *126*, 5138–5153.

[27] P. Singh, B. Sarkar, M. Sieger, M. Niemeyer, J. Fiedler, S. Záliš, W. Kaim, *Inorg. Chem.* **2006**, *45*, 4602–4609.

[28] F. Roncaroli, M. Videla, L. D. Slep, J. A. Olabe, *Coord. Chem. Rev.* **2007**, *251*, 1903–1930.

[29] O. V. Sizova, A. Y. Sokolov, L. V. Skripnikov, V. I. Baranovski, *Polyhedron* **2007**, *26*, 4680–4690.

[30] M. Radoń, K. Pierloot, *J. Phys. Chem. A* **2008**, *112*, 11824–11832.

[31] G. Tamasi, M. Curci, F. Berrettini, N. Justice, A. Sega, L. Chiasserini, R. Cini, *J. Inorg. Biochem.* **2008**, *102*, 1874–1884.

[32] G. F. Caramori, G. Frenking, *Croat. Chem. Acta* **2009**, *82*, 219–232.

[33] M. Radoń, E. Broclawik, K. Pierloot, *J. Phys. Chem. B* **2010**, *114*, 1518–1528.

[34] A. G. De Candia, J. P. Marcolongo, R. Etchenique, L. D. Slep, *Inorg. Chem.* **2010**, *49*, 6925–6930.

[35] P. Surawatanawong, S. Sproules, F. Neese, K. Wieghardt, *Inorg. Chem.* **2011**, *50*, 12064–12074.

[36] P. De, S. Maji, A. D. Chowdhury, S. M. Mobin, T. K. Mondal, A. Paretzkic, G. K. Lahiri, *Dalton Trans.* **2011**, *40*, 12527–12539.

[37] J. P. da Silva, F. R. Caetano, D. A. Cavarzan, F. D. Fagundes, L. L. Romualdo, J. Ellena, M. Jaworska, P. Lodowski, A. Barison, M. P. de Araujo, *Inorg. Chim. Acta* **2011**, *373*, 8–18.

[38] M. A. Jakupec, E. Reisner, A. Eichinger, M. Pongratz, V. B. Arion, M. Galanski, C. G. Hartinger, B. K. Keppler, *J. Med. Chem.* **2005**, *48*, 2831–2837.

[39] R. Ponec, *J. Math. Chem.* **1997**, *21*, 323–333.

[40] R. Ponec, *J. Math. Chem.* **1998**, *23*, 85–103.

[41] R. Ponec, A. Duben, *J. Comput. Chem.* **1999**, *8*, 760–771.

[42] R. F. W. Bader, *Atoms in Molecules: A Quantum Theory*, Clarendon Press, Oxford, **1990**.

[43] P. L. Popelier, *Atoms in Molecules: An Introduction*, Prentice Hall, London, **2000**.

[44] E. Tfouni, M. Krieger, B. R. McGarvey, D. W. Franco, *Coord. Chem. Rev.* **2003**, *236*, 57–69.

[45] J. A. McCleverty, *Chem. Rev.* **2004**, *104*, 403–418.

[46] Y. Cheng, F.-T. Lin, R. E. Shepherd, *Inorg. Chem.* **1999**, *38*, 973–983.

[47] J. Bultitude, L. F. Larkworthy, J. Mason, D. C. Povey, B. Sandell, *Inorg. Chem.* **1984**, *23*, 3629–3633.

[48] J. Mason, L. F. Larkworthy, E. A. Moore, *Chem. Rev.* **2002**, *102*, 913–934.

[49] E. C. Wasinger, M. I. Davis, M. Y. M. Pau, A. M. Orville, J. M. Zaleski, B. Hedman, J. D. Lipscomb, K. O. Hodgson, E. I. Solomon, *Inorg. Chem.* **2003**, *42*, 365–376.

[50] K. W. Hyung, T. Y. Kwon, Y. Jeon, *Solid State Commun.* **2003**, *125*, 259–264.

[51] M. Sikora, C. J. Oates, W. Szczerba, Cz. Kapusta, J. Zukrowski, D. A. Zajac, M. Borowiec, P. Ruiz-Bustos, P. D. Battle, M. J. Rosseinsky, *J. Alloys Compd.* **2007**, *442*, 265–267.

[52] I. Arcon, A. Bencan, M. Kosec, *X-Ray Spectrum.* **2007**, *36*, 301–304.

[53] M. Newcomb, J. A. Halgrimson, J. H. Horner, E. C. Wasinger, L. X. Chen, S. G. Sligar, *Proc. Natl. Acad. Sci. USA* **2008**, *105*, 8179–8184.

[54] V. Petrykin, Z. Bastl, J. Franc, K. Macounova, M. Makarova, S. Mukerjee, N. Ramaswamy, I. Spirovova, P. Krtil, *J. Phys. Chem. C* **2009**, *113*, 21657–21666.

[55] N. C. Pramanic, S. Bhattacharya, *J. Chem. Res. Synop.* **1997**, 98–99.

[56] M. Breza, P. Májek, *Polyhedron* **2007**, *26*, 4156–4160.

[57] M. Gall, M. Breza, *Polyhedron* **2009**, *28*, 521–524.

[58] S. Šoralová, M. Breza, *Polyhedron* **2010**, *29*, 2440–2444.

[59] P. Macchi, A. Sironi, *Coord. Chem. Rev.* **2003**, *238–239*, 383–412.

[60] P. Macchi, A. Sironi, *Interactions Involving Metals – From Chemical Categories to QTAIM and Backwards*, in: *The Quantum Theory of Atoms in Molecules* (Ed.: C. F. Matta, R. J. Boyd), Wiley, Weinheim, Germany, **2007**, p. 345.

[61] F. Cortés-Guzmán, R. F. W. Bader, *Coord. Chem. Rev.* **2005**, *249*, 633–662.

[62] C. Foroutan-Nejad, G. H. Shafiee, A. Sadjadi, S. Shahbazian, *Can. J. Chem.* **2006**, *84*, 771–781.

[63] X. Fradera, R. F. W. Bader, M. Austem, *J. Phys. Chem. A* **1999**, *103*, 304–314.

[64] R. Bochicchio, R. Ponec, L. Lain, A. Torre, *J. Phys. Chem. A* **2000**, *104*, 9130–9135.

[65] R. Ponec, F. Uhlík, *J. Mol. Struct.* **1997**, *391*, 159–168.

[66] R. Ponec, I. Mayer, *J. Phys. Chem. A* **1997**, *101*, 1738–1741.

[67] R. Bochicchio, R. Ponec, A. Torre, L. Lain, *Theor. Chem. Acc.* **2001**, *105*, 292–298.

[68] T. Kar, E. Sanchez-Marcos, *Chem. Phys. Lett.* **1992**, *192*, 15–20.

[69] A. B. Sannigrahi, T. Kar, *Chem. Phys. Lett.* **1990**, *173*, 569–572.

[70] K. C. Mundim, M. Giambiagi, M. S. Giambiagi, *J. Phys. Chem. A* **1994**, *98*, 6118–6119.

[71] V. A. Emelyanov, S. A. Gromilov, I. A. Baidina, A. V. Virovets, A. V. Belyaev, V. A. Logvinenko, *J. Struct. Chem.* **1999**, *40*, 883–891.

[72] *SAINT-Plus*, v. 7.06a, Bruker–Nonius AXS Inc., Madison, WI, **2004**; *APEX2*, Bruker–Nonius AXS Inc., Madison, WI, **2004**.

[73] G. M. Sheldrick, *Acta Crystallogr., Sect. A* **2008**, *64*, 112–122.

[74] E. Keller, *SCHAKAL-97*, Kristallographisches Institut, University of Freiburg, Germany, **1997**.

[75] B. Ravel, M. Newville, *J. Synchrotron Radiat.* **2005**, *12*, 537–541.

[76] Real Space Multiple Scattering Calculation of XANES, see: A. L. Ankudinov, B. Ravel, J. J. Rehr, S. D. Conradson, *Phys. Rev. B* **1998**, *58*, 7565–7576.

[77] A. D. Becke, *J. Chem. Phys.* **1993**, *98*, 5648–5652.

[78] M. T. Cancès, B. Mennucci, J. Tomasi, *J. Chem. Phys.* **1997**, *107*, 3032–3041.

[79] P. J. Hay, W. R. Wadt, *J. Chem. Phys.* **1985**, *82*, 299–310.

[80] L. E. Roy, P. J. Hay, R. L. Martin, *J. Chem. Theory Comput.* **2008**, *4*, 1029–1031.

[81] T. H. Dunning, Jr, *J. Chem. Phys.* **1989**, *90*, 1007–1023.

[82] D. E. Woon, T. H. Dunning Jr., *J. Chem. Phys.* **1993**, *98*, 1358–1371.

[83] M. Douglas, N. M. Kroll, *Ann. Phys.* **1974**, *82*, 89–155.

[84] B. A. Hess, *Phys. Rev.* **1985**, *A32*, 756–763.

[85] A. Wolf, M. Reiher, B. A. Hess, *J. Chem. Phys.* **2002**, *117*, 9215–9226.

[86] M. Reiher, A. Wolf, *Relativistic Quantum Chemistry*, Wiley-VCH, Weinheim, Germany, **2009**.

[87] F. Neese, A. Wolf, M. Reiher, T. Fleig, B. A. Hess, *J. Chem. Phys.* **2005**, *122*, 204107-(1–10).

[88] K. G. Dyall, *Theor. Chem. Acc.* **2004**, *112*, 403–409 (available at http://dirac.chem.sdu.dk).

[89] W. J. Hehre, R. Ditchfield, J. A. Pople, *J. Chem. Phys.* **1972**, *56*, 2257–2261.

[90] J. Frisch, G. W. Trucks, H. B. Schlegel, G. E. Scuseria, M. A. Robb, J. R. Cheeseman, J. A. Montgomery Jr., T. Vreven, K. N. Kudin, J. C. Burant, J. M. Millam, S. S. Iyengar, J. Tomasi, V. Barone, B. Mennucci, M. Cossi, G. Scalmani, N. Rega, G. A. Petersson, H. Nakatsuji, M. Hada, M. Ehara, K. Toyota, R. Fukuda, J. Hasegava, M. Ishida, T. Nakajima, Y. Honda, O. Kitao, H. Nakai, M. Klene, X. Li, J. E. Knox, H. P. Hratchian, J. B. Cross, C. Adamo, J. Jaramillo, R. Gomperts, R. E. Strat-mann, O. Yazyev, A. J. Austin, R. Cammi, C. Pomelli, J. W. Ochterski, P. Y. Ayala, K. Morokuma, G. A. Voth, P. Salvador, J. J. Dannenberg, V. G. Zakrzewski, S. Dapprich, A. D. Daniels, M.-C. Strain, O. Farkas, D. K. Malick, A. D. Rabuck, K. Raghavachari, J. B. Foresman, J. V. Ortiz, Q. Cui, A. G. Baboul, S. Clifford, J. Cioslowski, B. B. Stefanov, G. Liu, A. Liashenko, P. Piskorz, I. Komaromi, R. L. Martin, D. J. Fox, T. Keith, M. A. Al-Laham, C. Y. Peng, A. Nakaryakkara, M. Chalacombe, P. M. W. Gill, B. Johnson, W. Chen, M. W. Wong, C. Gonzales, J. A. Pople, *Gaussian 03*, rev. C.02, Gaussian, Inc., Wallingford, CT, **2004**.

[91] F. Feixas, X. Girones, R. Ponec, J. Roithova, *WinBader*, v1.0, ICPF, AS CR, Prague, Czech Republic, **2003** (available upon request, contact: PONEC@icpf.cas.cz).

[92] T. A. Keith, *AIMAll*, v. 11.12.19, TK Gristmill Software, Overland Park KS, **2011** (aim.tkgristmill.com).

[93] F. Neese, *ORCA - an ab initio, DFT and semiempirical electronic structure package*, v. 2.8, rev. 2131, Institut für Physikalische und Theoretische Chemie, Universität Bonn, Germany, September **2010** (http://www.thch.uni-bonn.de/tc/orca/).

[94] The ORCA Program System, see: F. Neese, *WIREs Comput. Mol. Sci.* **2012**, *2*, 73–78.

[95] L. Laaksonen, *gOpenMol* (http://www.csc.fi/english/pages/g0penMol).

[96] Gaussian Inc., *GaussView*, 2.1, Semichem, Pittsburgh, **2000**.

[97] F. Lanucara, B. Chiavarino, M. E. Crestoni, D. Scuderi, R. K. Sinha, P. Maître, S. Fornarini, *Inorg. Chem.* **2011**, *50*, 4445–4452.

[98] R. Ponec, X. Girones, *J. Phys. Chem. A* **2002**, *106*, 9506–9511.

[99] R. Ponec, J. Roithova, X. Girones, G. Frenking, *Organometallics* **2004**, *23*, 1790–1796.

[100] R. Ponec, G. Yuzhakov, D. L. Cooper, *Theor. Chem. Acc.* **2004**, *112*, 419–430.

[101] R. Ponec, G. Lendvay, J. Chaves, *J. Comput. Chem.* **2008**, *29*, 1387–1398.

[102] R. Ponec, F. Feixas, *J. Phys. Chem. A* **2009**, *113*, 5773–5779.

[103] R. Ponec, L. Bučinský, C. Gatti, *J. Chem. Theory Comput.* **2010**, *6*, 3113–3121.

[104] HEKA Elektronik Dr. Schulze GmbH, *Pot-Pulse,* 8.53, Lambrecht/Pfalz, Germany, **2004−2008**.